Research Square

Preprints are preliminary reports that have not undergone peer review.
They should not be considered conclusive, used to inform clinical practice,
or referenced by the media as validated information.

Improved Electrocatalytic Nitrogen Reduction to Ammonia over Cu-Fe-Mn-Ni-Co High-Entropy Alloy Anchored on Activated Carbon

Rashi Jain
Indian Institute of Technology Kanpur
Naveen Kumar Verma
Rajasthan Technical University
Rahul Gupta
Indian Institute of Technology Kanpur
Basker Sundararaju
Indian Institute of Technology Kanpur
NISHITH VERMA
VERMANISHITH@GMAIL.COM
Indian Institute of Technology Kanpur

Research Article

Keywords: High entropy alloy, Activated carbon substrate, Electrocatalyst, Electrochemical nitrogen reduction reaction (eNRR), Ammonia production

Posted Date: November 26th, 2026

DOI: https://doi.org/10.21203/rs.3.rs-11773211/v1

License: This work is licensed under a Creative Commons Attribution 4.0 International License.
Read Full License

Additional Declarations: No competing interests reported.

Abstract

Electrochemical nitrogen reduction reaction (eNRR) under atmospheric conditions is a sustainable substitute for traditional ammonia production techniques. This study reports an efficient eNRR performed over a cost-efficient, noble metal-free high-entropy alloy (HEA), comprising Cu, Fe, Mn, Ni, and Co (CFMNC), anchored on activated carbon particles (ACP). The CFMNC/ACP electrocatalyst is synthesized via suspension polymerization with the *in situ* addition of the respective metal nitrates at the onset of polymeric gel formation, followed by thermal processing. The physicochemical characterization tests confirm the formation of HEA with a configurational entropy of 1.58 R and the composition of each constituent metal within 5–35 mol%, satisfying the necessary and sufficient conditions for HEA formation. CFMNC/ACP demonstrates an enhanced eNRR activity with the NH_3 production rate of 33.82 $\mu g.h^{-1}.mg_{cat}^{-1}$ and Faradaic efficiency of 26.39% at -0.30 V vs RHE in 0.1 M KOH electrolyte. The catalyst showed a stable eNRR activity over eight consecutive cycles with less than 4% decline measured in the electrocatalytic activity. The significantly high eNRR activity of CFMNC/ACP is ascribed to the synergistic interactions between HEA nanoparticles and ACP. This study demonstrates a scalable and energy-efficient strategy for sustainable NH_3 production over noble metal-free HEA electrocatalyst.

1 Introduction

Ammonia (NH_3) is an indispensable chemical used in agriculture, industrial manufacturing, and emerging energy technologies. In addition to serving as a precursor to producing primary nitrogenous fertilizers, NH_3 is extensively utilized in the synthesis of explosives, fibers, plastics, and pharmaceuticals [1]. NH_3 has also gained substantial attention as a carbon-free energy vector and efficient hydrogen carrier for clean energy storage and transport [2]. NH_3-production remains predominantly reliant on the Haber-Bosch process. The process takes an energy-demanding thermochemical route that operates under extreme temperature (350–500°C) and pressure (150–350 atm) conditions using Fe- or Ru-based catalysts. The process accounts for nearly 1–2% of global energy consumption and annually contributes more than 1 Gt of carbon dioxide emissions [3, 4]. Such fossil-fuel dependence and harsh operating conditions have intensified the pursuit of alternative green and energy-efficient NH_3 synthesis pathways. The electrochemical nitrogen reduction has emerged as a viable route for NH_3 production under atmospheric conditions.

Electrochemical nitrogen reduction reaction (eNRR) involves the transformation of nitrogen to NH_3 through proton-coupled electron transfer steps at the active catalytic sites. Practical implementation of eNRR remains challenging because of the factors such as the exceptionally strong N ≡ N triple bond (941 kJ mol^{-1}), sluggish reaction kinetics, and a relatively low N_2 solubility in aqueous electrolytes. Moreover, NH_3-formation is often hindered by competing cathodic reactions, including hydrogen evolution reaction (HER) and hydrazine (N_2H_4) formation, thereby reducing overall NH_3 selectivity [5]. Overcoming these limitations is critical for improving the overall efficiency of eNRR.

Addressing these challenges, various advanced electrocatalysts have been explored, particularly using noble metals [6]. eNRR studies have also focused on noble metal-based systems. Salient among such studies, Feng et al. synthesized Ru single atoms decorated on a graphdiyne/graphene sandwiched structure [7]. Ru sites served as the primary N_2 activation centers, while hydrogen radicals, generated on graphdiyne, facilitated efficient hydrogenation. Liu et al. developed a Ru-Mn bimetallic electrocatalyst supported on porous carbon [8]. The electrocatalyst was synthesized via chemical vapor deposition technique. The inclusion of Mn significantly enhanced NH_3 formation rate from 123.73 to 187.06 $\mu g.h^{-1}.mg_{cat}^{-1}$. The improvement in the eNRR activity was ascribed to the Mn-induced electronic structure modulation of Ru. Additionally, the porous, electroconductive carbon support increased the surface area and facilitated electron transport. Although these electrocatalysts exhibit good performance, their reliance on noble metals limits the economic viability and scalability for large-scale applications.

The limitation has prompted growing interest towards the development of earth-abundant transition metals-based electrocatalysts (viz. Ti, Mn, Cr, Nb, V, Ce, Co, Ni, Cu, and Fe). Cai et al. reported Ni-Co bimetallic nanoparticles (NPs) supported on carbon nanosheets. The electrocatalyst was synthesized using modified Hummer's method. Ni and Co synergistically enhanced the e^- transport and density of active sites. The electrocatalyst achieved NH_3 formation rate and faradaic efficiency (FE) of 22.18 $\mu g\ h^{-1}mg_{cat}^{-1}$ and 4.5%, respectively [9]. Arif et al. constructed a CoFeB/rGO heterostructured electrocatalyst. The Co and Fe metal sites facilitated electron transfer to N_2, thereby weakening the N ≡ N bond [10]. Co sites exhibited the relatively stronger adsorption capacity and lower energy barrier, while the Fe sites facilitated the charge transfer. Cui et al. synthesized the Cu and Mn bimetallic nanoporous alloy using arc melting method [11]. Cu enhanced the electronic conductivity and provided N_2 adsorption sites, while Mn tuned the electronic properties of Cu, thereby enhancing the N_2 activation and facilitating subsequent hydrogenation steps. The synergistic interaction between Cu and Mn relatively reduced the overall reaction energy barrier, suppressing HER. The electrocatalyst exhibited the NH_3 formation rate of ~ 28 $\mu g\ h^{-1}.cm^{-2}$ and 9.8 % FE. Althugh bimetallic alloys have gained attention as an effective platform for eNRR through synergistic electronic effects, an extension beyond such conventional bimetallic systems opens a new avenue for electrocatalytic activities, attracting growing interest among the researchers and scientists.

High-entropy alloys (HEAs) represent an evolution in this direction. Such multi-metal systems are typically classified by (1) the composition of 5–35% (near equimolar) five or more metals and (2) the total configurational entropy (ΔS_{conf}) $\geq$ 1.5 R [12, 13]. To date, there are a few reported studies of the emerging HEA-based electrocatalysts applied to eNRR. Zhang et al. have developed an HEA of Ru, Fe, Co, Ni, and Cu [14]. The electrocatalyst delivered a relatively high NH_3 production rate of 57.1 $\mu g\ h^{-1}.mg_{cat}^{-1}$ (11.4 $\mu g\ h^{-1}\ cm^{-2}$) with a 38.5% FE at the overpotential of 0.05 V, combinedly attributed to Fe sites facilitating the N_2 adsorption and activation, and the Co-Cu and Ni-Ru pairs facilitating hydrogenation and efficient interfacial hydrogen transfer. Yu et al. used DFT calculations to study the synergistic effect of multi-element interactions on the electrocatalytic activity of a HEA synthesized from

Fe, Co, Ni, Cu, and Pd [15]. Specifically, the calculations showed improvement in the materials stability with increase in the Ni and Cu amounts. Fe atoms served as the primary active sites by donating electrons to the adsorbed N_2, facilitating its activation during eNRR. Christensen et al. synthesized a HEA of Au, Co, Fe, Mo, and Ru.[16] The HEA exhibited up to a two-fold higher activity compared to the monometallic electrocatalysts, the higher activity attributed to the diverse local atomic environments inherent to the multicomponent alloys. From these overviews, it is clear that the development of (noble metal-free) HEA as the electrocatalyst, especially for eNRR has not been studied fully. It is the focus of the present study.

The present study describes the synthesis of five transition metals, namely, Cu, Fe, Mn, Ni, and Co (CFMNC)-based HEA, anchored on activated carbon particles (ACP), for eNRR. The synergistic interaction among these earth-abundant metals is expected to generate the multiple active sites, optimized adsorption energies, and improved catalytic selectivity. Activated carbon has been widely used as a catalyst-substrate because of the materials large specific surface area, good electrical conductivity, chemical stability, and amenable to functionalization [17–20]. The electrocatalyst is synthesized via the suspension polymerization of phenol-formaldehyde copolymers, followed by the *in situ* addition of metal nitrate salts at the incipience of polymeric gel formation, and subsequent thermal treatment. CFMNC/ACP is systematically characterized using the various physicochemical and electrochemical techniques including scanning electron microscopy (SEM), transmission electron microscopy (TEM), X-ray photoelectron spectroscopy (XPS), electrochemical surface area (ECSA) analyzer, N_2-temperature programmed desorption (TPD), and electrical impedance spectroscopy (EIS). The ΔS_{conf} is calculated based on the HEA-carbon composite compositions determined using inductively coupled plasma mass spectrometry (ICP-MS). The eNRR activity is determined using linear sweep voltammetry (LSV) and chronoamperometry. Isotope labelling is performed to confirm the source of nitrogen used in the ammonia synthesis.

2 Materials and Methods

2.1 Chemicals

The study used all analytical-grade chemical reagents, which were applied as received without any pretreatment. A detailed list of chemicals with their suppliers is available in supplementary information (SI) file. N_2, H_2, and Ar gases (each 99.99% pure) were purchased from Sigma Gases, India. All solutions were prepared in Milli-Q (Merck, Germany) water.

2.2 Synthesis of CFMNC/ACP

The material was synthesized following a previously reported protocol, with slight modifications [17, 21]. Briefly, the polymerization reaction was performed in a three-necked round bottom glass reactor integrated with a condenser reflux assembly, stirrer, and temperature controller. Phenol (50 mL) and formaldehyde (63 mL), used as monomers, were mixed with 2 mL of triethylamine (TEA) used as the

polymerization catalyst. The solution was continuously stirred at 250 rpm for 60 min at 25 ^{o}C. Next, 200 mL of water was added and the solution was stirred for another 60 min. 6 g HMTA as a cross-linking agent was added, and the temperature was raised to 96°C. After 15 min, 3.5 g PVA was introduced as a suspension stabilizer to prevent the agglomeration of particles formed in the reaction. The solution color changed from pale to turbid yellow during polymerization. A 20 mL equimolar multi-metal salt solution (composition is described in Table S1) was added at the incipience of the polymeric gel (slurry) formation to avoid the formation of polymer-lump at a later stage. The suspension was cooled, and the formed polymeric beads in the spent reaction mixture were separated by sieving, followed by repeated washing with water. Figure 1 describes a schematic of the electrocatalyst synthesis procedure used in this study. The synthesized beads were powdered in a planetary ball mill (Retsch PM100, Germany) using zirconia balls (10 mm diameter, 20 pieces) at 350 rpm for 1.5 h. The powder was subjected to carbonization in a horizontal tubular furnace in N_2 (150 sccm). The carbonization step was performed at 900°C for 120 min, leading to the conversion of the polymer matrix to carbon particles and that of the metal nitrate salts to the respective metal oxides. The metal oxides-carbon particles were subjected to steam-activation at 900°C for 60 min in a mixture of steam and N_2 at 50 and 150 sccm, respectively. The steam-activation step resulted in the development of a porous structure and increase in the specific surface area (S_{BET}), discussed later in detail. Next, the activated sample was subjected to a thermal reduction step using H_2 (150 sccm) at 900°C for 2 h. This step resulted in the reduction of the metal oxides to zero-valent metals, confirmed later from the XPS and XRD analyses. Fig. S1 shows the hydrodynamic particle size distribution of CFMNC/ACP before and after thermal treatment, measured using a laser particle size analyzer (Microtrac Bluewave, USA). The average hydrodynamic particle size was found to decrease from 6.8 µm before thermal treatment to 5.5 µm after thermal treatment. CFMNC (without ACP) and ACP (without CFMNC) were also separately synthesized for comparison. CFMNC was prepared directly by drying the aqueous metal salt solutions, ball milling, and thermal treatment, i.e. without using the polymerization step. ACP was synthesized using the same procedure as that for CFMNC/ACP, however, without adding metal salts.

2.3 Electrochemical Setup and Working Electrode Preparation

All electrochemical experiments were carried out on an electrochemical workstation (Squidstat Plus, Admiral Instruments, USA). The workstation constituted the following components: (a) a three-electrode system comprising of Pt mesh, Ag/AgCl electrode, and a catalyst-coated glassy carbon electrode (GCE), as counter-, reference-, and working electrode, respectively, and (b) an H-cell (gas-tight) setup consisting of an anodic chamber, cathodic chamber, and separator (Nafion 117 ion exchange membrane). Both chambers were filled with identical electrolyte solutions. The Ag/AgCl electrode and catalyst-coated GCE were positioned in the cathodic compartment, while the platinum mesh was kept in the anodic compartment. The eNRR activity of the catalyst was determined in different electrolytes: 0.1 M solutions of KOH, HCl, and Na_2SO_4. The cathodic chamber was purged with Ar for 0.5 h to eliminate dissolved gases, prior to each experiment. Subsequently, N_2 gas was purged in the cathodic chamber to initiate

eNRR. Approximately 5 mg powdery electrocatalyst was added in the mixture of 980 and 20 µL of C_2H_5OH and Aquivion solution, respectively. The suspension was sonicated in an ultrasonic bath for 0.5 h. Next, 10 µL electrocatalyst ink was drop-cast on GCE (3 mm diameter). Fig. S2 presents the digital photograph of the workstation and H-cell setup used in this study.

2.4 Electrochemical Measurements

Polarization curves were recorded using LSV at a scan rate of 1 mV s^{-1} over the potential window of -1.0–0.0 V vs. RHE. Chronoamperometric measurements were also taken at different potentials for a fixed duration of 1 h. EIS data were collected at open circuit potential (OCP) across the frequency range of 10^5 – 10^{-3} Hz in 0.1 M Na_2SO_4 electrolyte. The Nernst equation (S1) was used for converting the measured electrode voltages to the RHE scale. ECSA was determined using the cyclic voltammetry (CV) experimental data. CV experiments were performed in 5 mM $K_3Fe(CN)_6$ solution at different scan rates ranging from 0.01 to 100 mV in the potential window of -0.5–1.0 V vs. Ag/AgCl. All the experiments were carried out in triplet to ensure the reproducibility.

2.5 NRR Product Quantification

The major liquid products of eNRR i.e., NH_3 and N_2H_4 were quantified using Nessler's reagent method and Watt and Chrisp method, respectively [22–24]. The detailed procedures for the NH_3 and N_2H_4 measurements are provided in sections S2 and S3. The calibration plots for NH_3 and N_2H_4 are shown in Fig. S3. The gaseous products evolved during eNRR were quantified by thermal conductivity detector attached to a gas chromatography (Trace 1110, Thermo Fisher Scientific, USA).

3 Results and Discussion

3.1 Physicochemical Characterization

The surface and internal morphology of CFMNC and CFMNC/ACP are visualized using the SEM and TEM images. Fig. S4a shows the SEM image of CFMNC. Figure 2(a-c) show the SEM images of CFMNC/ACP, recorded at successively higher magnifications. The images reveal the morphology of spherical HEA NPs in the relatively brighter particles anchored on black activated carbon. A uniform distribution of the NPs without agglomeration indicates an effective anchoring of the CFMNC HEA NPs on ACP. The TEM image of CFMNC/ACP reveals the relatively darker spherical HEA NPs distributed over a relatively lighter carbonaceous ACP substrate (Fig. 2d). Figure 2(e and f) display the high-resolution TEM (HR-TEM) images of CFMNC/ACP, revealing well-defined lattice fringes (analyzed using ImageJ software) and confirming a highly ordered crystalline structure. The measured interplanar spacing of ~ 2.05 Å is assigned to the (1 1 1) lattice plane of CFMNC in CFMNC/ACP [25]. This lattice plane is also consistent with the XRD results, discussed later.

The surface elemental composition of the electrocatalysts were determined using energy dispersive X-ray spectroscopy (EDS) analysis. Figure 2g and S4b show the EDS spectra of CFMNC/ACP and CFMNC, respectively. The presence of Cu, Fe, Mn, Ni, Co, and C elements was confirmed in the EDS spectra of CFMNC/ACP. Table S2 shows the composition of constituent elements at the electrocatalyst surface. The inset table displays the surface elemental composition, indicating the metal contents varying between 14.87 and 26.02 mol% (Fig. 2g'). The overall metal content of CFMNC/ACP was further quantified by the ICP-MS analysis. The molar composition of the constituent metals is presented in Table S3. Ni and Fe exhibit the lowest and highest atomic fractions of 14.6 and 26.8%, respectively. The compositional values determined from the ICP-MS analysis are in close agreement with those determined from EDS. Notably, the measured atomic ratios fulfill a key requirement for HEAs, with each constituent element within the 5–35% atomic composition range [12]. In comparison, the atomic composition of CFMNC (without carbon support) exhibits a much wider variation, with the metal contents ranging from 2.7 (Co) to 48.5% (Cu).

The ΔS_{conf} of the synthesized electrocatalysts was determined using the ICP-MS data and equation S2 [26]. The calculated ΔS_{conf} value for CFMNC/ACP was found to be 1.58 *R*, which exceeds the critical threshold of 1.5 *R* ($\Delta S_{conf} \geq 1.5\ R$), thereby satisfying the fundamental criterion for the HEA formation [27]. In contrast, the unsupported CFMNC sample exhibits a relatively lower mixing entropy ($\Delta S_{conf} = 1.18\ R$), ascribed to elemental segregation occurring at the relatively high temperature in the absence of the ACP substrate [17, 28]. Figure 2 (h-m) show the SEM-EDS elemental mapping of CFMNC/ACP. The mapping results revealed that the HEA constituent metals were uniformly distributed over ACP. The particle size distribution of the HEA NPs was plotted using ImageJ plotting software through the analysis of TEM images (Fig. S5). The average particle diameter was determined to be 106.2 nm, with the size ranging from 45 to 240 nm.

Figure 3a presents the XRD patterns of CFMNC, ACP, and CFMNC/ACP. The diffraction peaks at 23.5 and 42.9° are attributed to the (0 0 2) and (1 0 0) crystalline planes of graphitic carbon in ACP, respectively [29, 30]. The diffraction peaks in CFMNC at 43.8, 50.9, and 75.1° are attributed to the (1 1 1), (2 0 0), and (2 2 0) crystallite planes of the face-centered cubic structure, respectively [25, 31]. The XRD pattern of CFMNC/ACP displays the characteristic peaks of both ACP and CFMNC, indicating a strong interaction between the HEA NPs and carbon support.

The S_{BET} and pore structure of the synthesized electrocatalysts were determined using N_2 adsorption-desorption isotherms (Fig. 3b) and pore size distribution plot (Fig. S6a), respectively. The calculated S_{BET} values and total pore volumes of the synthesized electrocatalysts are compiled in Table S4. The S_{BET} values for ACP and CFMNC/ACP were determined to be ~ 1355 and 607.6 $m^2\ g^{-1}$, respectively. The similar trend was observed in the total pore volumes of ACP and CFMNC/ACP. The total pore volume decreased from 0.73 in ACP to 0.37 $cm^3\ g^{-1}$ in CFMNC/ACP, indicating the partial filling of ACP pores by HEA NPs. The S_{BET} and total pore volume of CFMNC were determined to be 33.2 $m^2\ g^{-1}$ and 0.02 $cm^3\ g^{-1}$, respectively, indicating a compact and nonporous structure of CFMNC. N_2-TPD analysis was performed

to determine the nitrogen adsorption characteristics and the strength of N_2-electrocatalyst surface interactions (BELCAT II, MicrotracBEL Corp., Japan) [32, 33]. The relatively lower temperature region (~ 50–170°C) is primarily associated with physisorption, whereas the higher-temperature region (~ 250–650°C) predominantly reflects chemisorption region (Fig. S6b). CFMNC/ACP exhibits a substantially stronger desorption response than ACP, particularly above 350°C, with two prominent peaks near 515 and 585°C. However, ACP displays a relatively weak, broad peak centered around 300°C, followed by a gradual decline in desorption intensity. These pronounced high-temperature peaks suggest the stronger N_2-surface interactions and presence of energetically distinct adsorption sites in CFMNC/ACP electrocatalyst. The enhanced N_2 adsorption characteristics facilitate N_2 activation and contribute to the improved electrochemical nitrogen reduction performance of CFMNC/ACP electrocatalyst.

Figure 3c presents the Raman spectra of the electrocatalysts. The ACP and CFMNC/ACP spectra showed bands centered at 1340.2 and 1581.6 cm^{-1} corresponding to the D- and G bands, respectively. The D and G bands correspond to sp^3-hybridized disordered carbon and the in-plane vibrational mode of sp^2-hybridized graphitic carbon, respectively [34]. The intensity of the G-band is higher than that of the D-band, corroborating that graphitic carbon is more dominant than amorphous carbon in ACP and CFMNC/ACP. The ratio of the D-band to G-band intensities (I_D/I_G) reflects the extent of defects and disorder within the carbon structure.[35] A slight decrease in the I_D/I_G value from 0.93 in ACP to 0.90 in CFMNC/ACP indicates an enhanced graphitization and improved electrical conductivity in CFMNC/ACP. The increased degree of graphitization in CFMNC/ACP is ascribed to the catalytic effects of the metal NPs [21, 36, 37]. The Raman spectra of CFMNC did not show any D and G bands, indicating the absence of graphitic carbon phase.

XPS was used to determine the chemical oxidation states of the constituent elements in CFMNC/ACP. The survey spectrum confirmed the presence of Cu, Fe, Mn, Ni, Co, and C (Fig. S6c). The high-resolution XPS spectra were deconvoluted using Gaussian functions. The Cu 2p spectrum exhibits peaks at 932.6 and 952.6 eV, attributed to metallic Cu^0 [38]. Additionally, the peaks centered at 933.4 and 942.8 eV are assigned to Cu^{2+} and a satellite peak, respectively (Fig. 3d). The ratio of the integrated peak areas corresponding to Cu^0 and Cu^{2+} was determined to be 1.22. The high-resolution Fe 2p spectrum exhibits peaks at 706.2 and 710.9 eV, assigned to metallic Fe^0 and Fe^{2+}, respectively (Fig. 3e) [39]. The integrated peak area associated with Fe^0 is 1.52 times that associated with Fe^{2+}. The Mn 2p spectrum displays peaks at 638.7 and 650.5 eV, attributed to metallic Mn^0, along with peaks at 641.2 and 653.3 eV assigned to 2 + oxidation state of Mn [40]. The relatively larger peak area associated with Mn^0 (3.96 and 1.52 times than Mn^{2+} and Mn^{3+}, respectively) indicates that metallic Mn is the predominant Mn species on the surface (Fig. 3f). The Ni 2p spectrum exhibits multiple peaks centered at 852.6, 855.7, 860.7, 863.9, 873.1, 874.9, and 878.3 eV, corresponding to metallic and oxidized Ni species and their associated satellite peaks (Fig. 3g) [39]. The peaks at 855.7 and 873.1 eV are assigned to Ni^{2+}, whereas the peaks at 852.6 and 874.9 eV are attributed to metallic Ni^0 and Ni^{3+}, respectively. The area ratios of Ni^0 to Ni^{2+} and Ni^0 to Ni^{3+} were determined to be approximately 1.52 and 3.22, respectively. The Co 2p spectrum

exhibits a peak at 778.5 eV, characteristic of metallic Co^0 (Fig. 3h) [17, 41]. The peaks at 780.8 and 796.6 eV are assigned to Co^{2+}, while those at 784.4 and 802.4 eV correspond to satellite peaks. The peak area of Co^0 was ~ 1.22 times that of Co^{2+}.The high-resolution C 1s spectrum was deconvoluted to three peaks. The peak at 284.8 eV is assigned to sp^2-hybridized graphitic carbon, indicating the presence of a conductive carbon framework. The additional peaks at 285.4 and 288.9 eV are attributed to sp^3-hybridized carbon and carbonyl (C = O) groups, respectively [42]. The O 1s spectrum exhibit peaks at binding energies corresponding to 532.3 and 533.5 eV, assigned to metal-oxygen and oxygen-containing carbon bonds, respectively (Fig. S6d) [43]. Overall, the XPS results indicate the coexistence of metallic and oxidized surface species, with the relative contributions varying among the five metals. The detection of oxidized species is consistent with partial surface oxidation following exposure to air, while the metallic-state signals support the presence of a predominantly metallic Cu-Fe-Mn-Ni-Co HEA anchored on porous ACP. These findings are consistent with the XRD analysis.

3.2 Electrochemical Study

EIS analysis was performed to understand the interfacial charge transfer characteristics of the electrocatalysts. Nyquist plots were constructed from the recorded EIS data (Fig. 4a). Table S5 lists the kinetic parameters, namely, solution resistance (R_s), charge-transfer resistance (R_{ct}), and Warburg diffusion resistance (R_w), determined by fitting the EIS data to equivalent Randles circuit.

The identical R_s values (~ 51 Ω) for each electrocatalyst clearly indicate that the identical electrolyte conditions were maintained throughout the EIS experiments. The R_{ct} values for CFMNC/ACP, CFMNC, and ACP were measured to be ~ 15.0, 47.4, and 70.0 Ω, respectively. The lowest R_{ct} value for CFMNC/ACP indicates a relatively more efficient electron transport, ascribed to the synergistic interaction of HEA NPs with ACP. CFMNC/ACP exhibits the steepest slope in the linear region at low frequencies, indicating fastest ion transport [44]. The improved mobility of both the ions and electrons is beneficial for achieving an improved eNRR performance.

ECSA of the synthesized electrocatalysts were calculated using Randles-Sevcik equation, discussed in SI [20]. Figure 4(b-d) show the CV curves recorded at different scan rates for CFMNC/ACP, ACP, and CFMNC, respectively. Figure 4(b'-d') show the plot of anodic- and cathodic- peak currents versus the square root of the scan rates. The peak current vs $(\text{scan rate})^{1/2}$ exhibited a linear relationship (R^2 = 0.99), indicating the diffusion-controlled electron transfer process [45]. The ECSAs values for CFMNC/ACP, CFMNC, and ACP were determined to be 9.14, 0.43, and 0.24 cm^2 `cm^{-2} of the geometrical surface area of GCE, respectively. The highest ECSA of CFMNC/ACP confirms the presence of the relatively higher electrochemically active sites compared to the other synthesized electrocatalysts in the study.

Figure 5a and 5b present the LSV data recorded for CFMNC/ACP under the Ar and N_2 saturated conditions in different electrolytes viz. 0.1 M solution of KOH (basic), HCl (acidic), and Na_2SO_4 (neutral) each, at the scan rate of 1 mV/s. Measurements were taken at the constant gas

flow rate of 10 sccm. In each electrolyte, the current density is significantly higher when using N_2 than Ar, indicating the occurrence of an eNRR reaction [14]. The highest activity is observed in KOH, followed by Na_2SO_4 and HCl. The enhanced performance in the basic electrolyte indicates a favorable N_2 adsorption and the suppressed competing HER, leading to the improved eNRR selectivity. Figure 5c shows the LSV scans of ACP, CFMNC, and CFMNC/ACP in N_2 and Ar with 0.1 M KOH. CFMNC/ACP shows a significantly higher current density compared to CFMNC in N_2, indicating an enhanced eNRR activity attributed to the synergistic interaction between HEA and ACP. Figure 5d shows the Tafel plots recorded in the Ar-saturated 0.1 M electrolytes. CFMNC/ACP shows the highest slope in the basic electrolyte in comparison to the other electrolytes, and also, a higher slope than CFMNC, attributing to the suppressed HER activity of the electrocatalyst [46]. All subsequent experiments were performed in 0.1 M KOH unless explicitly mentioned otherwise.

The eNRR performance of CFMNC/ACP was determined using chronoamperometry measurements in an alkaline medium at various applied potentials for 3600 s. eNRR proceeds through spatially separated half-reactions at the electrodes [47, 48]. Hydroxide ions undergo oxidation at the anode, generating the electrons required for the reduction process (Eq. 1). N_2 is reduced to NH_3 at the cathode through a six-electron transfer pathway (Eq. 2).

$$6OH^- \rightarrow 3H_2O + 1.5O_2 + 6e^-$$

1

$$N_2 + 6H_2O + 6e^- \rightarrow 2NH_3 + 6OH^-$$

2

$$N_2 + 4H_2O + 4e^- \rightarrow N_2H_4 + 4OH^-$$

3

$$2H_2O + 2e^- \rightarrow H_2 + 2OH^-$$

4

$$N_2 + 3H_2O \rightarrow 2NH_3 + \frac{3}{2}O_2$$

5

FE for ammonia production is defined as the ratio of the electrical charge theoretically required for ammonia formation to the total electrical charge passed through the electrochemical system [49]. Figure 6a shows that the current densities increased with the increasing applied potentials. The NH_3 formation rate and FE are calculated using eq. S4 and eq. S5, respectively, and the results are presented in Fig. 6b. The electrocatalyst exhibited optimal performance at -0.3 V vs. RHE, achieving the ammonia

formation rate of 33.82 μg h^{-1} mg_{cat}^{-1} and FE of 26.39%. In addition to the NH_3 evolution, two competing reactions, namely, N_2H_4 formation and HER (Eqs. 3 and 4) may occur. However, no N_2H_4 was detected in the electrolyte, indicating an effective suppression of hydrazine generation step. H_2 is generated via the reduction of H_2O (Eq. 4). At the end of the reaction, a 1 mL gas sample was collected using a gas-tight syringe. The concentration of H_2 was quantified using GC.

Figure S7a compares the FE of H_2 and NH_3 across different applied potentials, highlighting their competitive relationship. At relatively less negative potentials (-0.1 to -0.3 V), HER dominates because of faster kinetics. At -0.3 V, a favorable N_2 activation leads to maximum NH_3 FE and suppressed HER. At negative potentials more than − 0.3 V, HER again becomes dominant, reducing NH_3 selectivity, which is consistent with the reported volcano-type behavior in the literature [50]. Eq. 5 represents the overall reaction showing the conversion of N_2 to NH_3. In addition to UV-Vis analysis, the NH_3 formation was also quantified using ion chromatography (IC, Fig. S7b), confirming the results consistent with those obtained from UV-Vis measurements. These findings demonstrate an excellent electrocatalytic performance and selectivity of CFMNC/ACP at -0.3 V towards eNRR.

Isotope labeling test using ^{15}N isotope was performed to confirm the formation of NH_3 and identify the nitrogen source (origin) of NH_3 using the ^1H nuclear magnetic resonance spectroscopy (NMR, Bruker Avance 500 spectrometer operating at 500 MHz) (Fig. 6c). $^{14}N_2$ and $^{15}N_2$ were purged separately in the electrolyte during the eNRR experiments. The collected sample was mixed with the solution of DMSO-d_6 and HCl (1:4, v/v). Figure 6c presents the ^1H NMR spectra recorded using $^{15}N_2$ feed gas. The spectra exhibited a characteristic doublet splitting with a coupling constant (J_{N-H}) of ~ 72.3 Hz, corresponding to the formation of $^{15}NH_4^+$. On the other hand, the spectra recorded using $^{14}N_2$ feed gas showed a triplet splitting pattern with the coupling constant of ~ 53.8 Hz, corresponding to the formation of $^{14}NH_4^+$ [51]. The distinct doublet and triplets observed in the ^1H NMR spectra of the electrolyte purged with $^{14}N_2$ and $^{15}N_2$, respectively, confirm that NH_3 primarily originated from the electrocatalytic reduction of the supplied N_2. A comparison of the electrochemical performance of our electrocatalyst (CFMNC/ACP) with the previously reported eNRR electrocatalysts is summarized in Table S6 [9, 14, 52–54]. The comparative data for the kinetic rate and FE confirm the suitability and effectiveness of CFMNC/ACP for NH_3 synthesis under atmospheric conditions.

Stability analysis was performed to assess the practical applicability of the electrocatalysts by performing eight consecutive eNRR cycles at -0.30 V vs RHE. A marginal decrease of less than 4% was observed in both the NH_3 formation rate and FE (Fig. 6d). Further, the structural and surface characteristics of the spent electrocatalyst were determined. The SEM image showed that the surface morphology of the spent CFMNC/ACP remained unaltered (Fig. S8a). EDS spectra and the corresponding elemental mapping confirmed that Cu, Fe, Mn, Ni, and Co remained uniformly distributed in the spent CFMNC/ACP catalyst (Fig. S8(b-h)). The atomic percentages of the constituent metals in the

spent catalyst were quantified by ICP-MS analysis, showing values in the range of 27.4% (Cu) – 13.7% (Co). The configurational entropy of the spent catalyst was determined to be 1.57 R, which is close to that of the fresh sample (1.58 R), also satisfying the required criterion for HEAs (Table S7).

Figure S9a displays the XRD patterns of the spent CFMNC/ACP electrocatalyst. The spent sample retains the characteristics of the FCC diffraction peaks corresponding to the (1 1 1), (2 0 0), and (2 2 0) crystallite planes, indicating that the crystalline structure remains preserved. The EIS spectra reveal a comparable Nyquist plot for both the fresh and spent electrocatalysts (Fig. S9b). The spent electrocatalyst exhibits an increased charge-transfer resistance compared to the fresh sample. XPS survey spectra confirm the Cu 2p, Ni 2p, Co 2p, Fe 2p, Mn 2p, O 1s, and C 1s signals in the spent catalyst, with negligible deviation in the peak positions (Fig. S9c). Overall, these results demonstrate that CFMNC/ACP is stable throughout the repeated eNRR cycles, demonstrating preserved catalytic activity, good structural integrity, and sustained selectivity. These results confirm a reliable operational stability of the electrocatalyst under prolonged electrochemical conditions.

4 Conclusions

A noble-metal-free CFMNC HEA supported on ACP was synthesized via a suspension polymerization-assisted *in situ* metal salt impregnation technique. The alloy exhibited a configurational entropy of 1.58 R, satisfying the essential criterion for HEA formation. The electrocatalyst demonstrated enhanced charge-transfer kinetics, relatively higher electrochemically active surface area, and an improved nitrogen adsorption characteristics. The enhanced nitrogen adsorption facilitated nitrogen activation and contributed to improved electrochemical nitrogen reduction performance. A maximum ammonia yield rate of 33.82 33.82 μg h^{-1} $mgcat^{-1}$ of catalyst and a Faradaic efficiency of 26.39% were achieved at − 0.3 V versus the RHE under ambient conditions, with the catalytic stability sustained over eight consecutive electrochemical nitrogen reduction cycles. The superior electrocatalytic performance is attributed to synergistic electronic interactions among the constituent transition metals and efficient electron transport through the conductive activated carbon support. This study highlights the potential of noble-metal-free, earth-abundant high-entropy alloy electrocatalysts for sustainable ammonia production through electrochemical nitrogen fixation.

Abbreviations

NH_3
Ammonia
eNRR
Electrochemical nitrogen reduction reaction
HER
Hydrogen evolution reaction
N_2H_4
Hydrazine

NPs
Nanoparticles
FE
Faradaic efficiency
HEA
High-entropy alloys
ΔS_{conf}
Total configurational entropy
CFMNC
Cu, Fe, Mn, Ni, and Co
ACP
Activated carbon particles
SEM
Scanning electron microscopy
TEM
Transmission electron microscopy
XPS
X-ray photoelectron spectroscopy
ECSA
Electrochemical surface area
TPD
Temperature programmed desorption
EIS
Electrical impedance spectroscopy
LSV
Linear sweep voltammetry
ICP-MS
Inductively coupled plasma mass spectrometry
SI
Supplementary information
TEA
Triethylamine
S_{BET}
Specific surface area
GCE
Glassy carbon electrode
OCP
Open circuit potential
CV
Cyclic voltammetry

EDS
Energy dispersive X-ray spectroscopy
R_s
Solution resistance
R_{ct}
Charge-transfer resistance
R_w
Warburg diffusion resistance
IC
Ion chromatography
NMR
Nuclear magnetic resonance spectroscopy

Declarations

Supplementary Information

The online version contains supplementary material available at...

Ethics and Consent to Participate Not applicable. This study did not involve human participants or animals.

Consent for Publication

Not applicable. The manuscript does not report identifiable individual human data, images, videos, or case reports.

Competing Interests

The authors declare that they have no competing interests.

Funding

This research was financially supported by the Ministry of Human Resource Development, Government of India (Grant No. SERB/ChE/2023772).

Author Contribution

R.J. and N.K.V. performed experiments, materials characterization, and wrote the original draft of manuscript. R.G. assisted in data analysis. B.S. investigated experiments and edited the manuscript. N.V. supervised, organized funding, and edited the manuscript. All authors reviewed the final manuscript.

Acknowledgments

The authors express their gratitude to the Department of Environmental Science and Engineering, Indian Institute of Technology Kanpur, India, for providing the research facilities.

Availability of Data and Materials

The data supporting the findings of this study and information regarding the materials used are available from the corresponding author upon request.

References

1. Liang Z, Liu C, Chen M et al (2020) Theoretical screening of di-metal atom (M = Fe, Co, Ni, Cu, Zn) electrocatalysts for ammonia synthesis. Int J Hydrogen Energy 45:31881–31891. https://doi.org/10.1016/j.ijhydene.2020.08.208
2. Joseph Sekhar S, Samuel MS, Glivin G et al (2024) Production and utilization of green ammonia for decarbonizing the energy sector with a discrete focus on sustainable development goals and environmental impact and technical hurdles. Fuel 360:130626. https://doi.org/10.1016/j.fuel.2023.130626
3. Chen S, Perathoner S, Ampelli C et al (2017) Electrocatalytic synthesis of ammonia at room temperature and atmospheric pressure from water and nitrogen on a carbon-nanotube-based electrocatalyst. Angew Chem Int Ed 56:2699–2703. https://doi.org/10.1002/anie.201609533
4. Kim K, Lee SJ, Kim D et al (2018) Electrochemical synthesis of ammonia from water and nitrogen: A lithium-mediated approach using lithium-ion conducting glass ceramics. Chemsuschem 11:120–124. https://doi.org/10.1002/cssc.201701975
5. Ismael M, Wark M (2024) A recent review on photochemical and electrochemical nitrogen reduction to ammonia: Strategies to improve NRR selectivity and faradaic efficiency. Appl Mater Today 39:102253. https://doi.org/10.1016/j.apmt.2024.102253
6. Lv X, Weng C, Yuan Z (2020) Ambient Ammonia Electrosynthesis: Current Status, Challenges, and Perspectives. Chemsuschem 13:3061–3078. https://doi.org/10.1002/cssc.202000670
7. Feng X, Liu J, Chen L et al (2023) Hydrogen radical-induced electrocatalytic N_2 reduction at a low potential. J Am Chem Soc 145:10259–10267. https://doi.org/10.1021/jacs.3c01319
8. Liu X, He N, Ni H et al (2024) Revolutionizing nitrogen electrocatalysis: Atomically dispersed ruthenium catalyzed by manganese for unmatched performance. Appl Catal Gen 688:119990. https://doi.org/10.1016/j.apcata.2024.119990
9. Cai J, Tian J, Abulizi A et al (2023) Two-dimensional carbon nanosheets loaded with NiCo bimetallic catalysts for efficient electrocatalytic reduction of nitrogen to ammonia. J Alloys Compd 958:170476. https://doi.org/10.1016/j.jallcom.2023.170476

10. Arif M, Kumar A, Asim Mushtaq M et al (2023) Edge-hosted CoFeB active sites with graphene nanosheets for highly selective nitrogen reduction reaction towards ambient ammonia synthesis. Chem Eng J 473:145368. https://doi.org/10.1016/j.cej.2023.145368
11. Cui Y, Dong A, Qu Y et al (2021) Theory-guided design of nanoporous CuMn alloy for efficient electrocatalytic nitrogen reduction to ammonia. Chem Eng J 426:131843. https://doi.org/10.1016/j.cej.2021.131843
12. Yeh J-W, Chen S, -K., Lin S, -J. et al (2004) Nanostructured high-entropy alloys with multiple principal elements: Novel alloy design concepts and outcomes. Adv Eng Mater 6:299–303. https://doi.org/10.1002/adem.200300567
13. Cantor B, Chang ITH, Knight P, Vincent AJB (2004) Microstructural development in equiatomic multicomponent alloys. Mater Sci amp 375–377:213–218. https://doi.org/10.1016/j.msea.2003.10.257
14. Zhang D, Zhao H, Wu X et al (2021) Multi-site electrocatalysts boost pH-universal nitrogen reduction by high-entropy alloys. Adv Funct Mater 31. https://doi.org/10.1002/adfm.202006939
15. Yu Y, Zhang W, Sun F et al (2022) High electrocatalytical performance of FeCoNiCuPd high-entropy alloy for nitrogen reduction reaction. Mol Catal 519:112141. https://doi.org/10.1016/j.mcat.2022.112141
16. Christensen O, Hutu A-I, Kristoffersen HH, Rossmeisl J (2024) N_2 dissociation on AuCoFeMoRu high-entropy alloys: Circumventing scaling relations and step dependencies. J Catal 436:115572. https://doi.org/10.1016/j.jcat.2024.115572
17. Verma NK, Gupta R, Verma N (2025) Carbon-supported noble metal-free high-entropy alloy: A new synthesis approach and application to hydrogen evolution reaction. Electrocatal 16:713–725. https://doi.org/10.1007/s12678-025-00953-7
18. Chai B, Miao L, Zhao N et al (2024) An effective carbon-supported high-entropy-alloy catalyst of PtPdNiCoBi for ethylene glycol electrooxidation. Catal Lett 154:6315–6320. https://doi.org/10.1007/s10562-024-04801-z
19. Tomar SS, Verma N, Nigam KDP (2025) Biogenic synthesis of the mixed-valence FexOy/g-CN electrocatalyst using coiled flow inverter for green hydrogen evolution. Chem Eng Process : Process Intensif 217:110503. https://doi.org/10.1016/j.cep.2025.110503
20. Santra T, Gupta R, Misra SK, Verma N (2025) Copper nanoparticle-dispersed laser-induced graphene film-based electrochemical sensor for thrombin in biomimic samples of hemophilia. ACS Appl Nano Mater 8:17567–17575. https://doi.org/10.1021/acsanm.5c03099
21. Verma NK, Sundararaju B, Verma N (2026) Electrochemical CO_2-reduction to formate over activated-carbon-supported transition metals (M = Cu, Fe, Zn, Ni, Co)-based high-entropy oxide. Electrocatal 17:84–98. https://doi.org/10.1007/s12678-025-00989-9
22. Araujo RG, Perez J (2025) Nitrogen electrochemical reduction reaction pathways evidenced by online electrochemical mass spectrometry and isotope labeling on the MoS_2 surface. ACS Electrochem 1:294–302. https://doi.org/10.1021/acselectrochem.4c00135

23. Song P, Wang H, Kang L et al (2019) Electrochemical nitrogen reduction to ammonia at ambient conditions on nitrogen and phosphorus co-doped porous carbon. Chem Commun 55:687–690. https://doi.org/10.1039/C8CC09256G
24. Gupta R, Alam U, Verma N (2024) Efficient photofixation of nitrogen to ammonia over an S-scheme-based $NiSnO_3$-g-C_3N_4 heterojunction. Chem Eng J 479:147644. https://doi.org/10.1016/j.cej.2023.147644
25. Huang K, Zhang B, Wu J et al (2020) Exploring the impact of atomic lattice deformation on oxygen evolution reactions based on a sub-5 nm pure face-centred cubic high-entropy alloy electrocatalyst. J Mater Chem Mater 8:11938–11947. https://doi.org/10.1039/D0TA02125C
26. Jin X, Zhou Y, Zhang L et al (2018) A new pseudo binary strategy to design eutectic high entropy alloys using mixing enthalpy and valence electron concentration. Mater Des 143:49–55. https://doi.org/10.1016/j.matdes.2018.01.057
27. Rius-Ayra O, Biserova-Tahchieva A, López-Jiménez I, Llorca-Isern N (2025) Degradation of methyl red at the surface of FeAlNiCuCo high-entropy alloys. Surf Interfaces 72:106959. https://doi.org/10.1016/j.surfin.2025.106959
28. Gerber IC, Serp P (2020) A Theory/Experience Description of support effects in carbon-supported catalysts. Chem Rev 120:1250–1349. https://doi.org/10.1021/acs.chemrev.9b00209
29. Zięzio M, Charmas B, Jedynak K et al (2020) Preparation and characterization of activated carbons obtained from the waste materials impregnated with phosphoric acid(V). Appl Nanosci 10:4703–4716. https://doi.org/10.1007/s13204-020-01419-6
30. Zhao L, Liu S, Wei L et al (2024) One-pot hydrothermal synthesis of bifunctional Co/Mo-rGO efficient electrocatalyst for HER/OER in water splitting. Catal Lett 154:5294–5302. https://doi.org/10.1007/s10562-024-04723-w
31. Zhao C, Cai W, Sun N et al (2024) Facile preparation of porous high-entropy alloy FeCoNiCuMn and its OER performance. J Phys Chem Solids 184:111668. https://doi.org/10.1016/j.jpcs.2023.111668
32. Lee J, Liu X, Kumar A et al (2021) Phase-selective active sites on ordered/disordered titanium dioxide enable exceptional photocatalytic ammonia synthesis. Chem Sci 12:9619–9629. https://doi.org/10.1039/D1SC03223B
33. Liu R, Guo T, Fei H et al (2022) Highly efficient electrocatalytic N_2 reduction to ammonia over metallic 1T phase of MoS_2 enabled by active sites separation mechanism. Adv Sci 9. https://doi.org/10.1002/advs.202103583
34. Singh Tomar S, Anand Omar R, Bhaduri B et al (2024) Denitrification using a novel Ni-CNF/g-C_3N_4 catalyst and nitrate-enriched wastewater-resourced *Achromobacter denitirificans*. Chem Eng Sci 285:119617. https://doi.org/10.1016/j.ces.2023.119617
35. Lin J, Lin X, Wang D et al (2025) One-step synthesis of armoured catalyst with ordered carbon layer coated FeCoNiCuZn high-entropy alloy for producing renewable hydrogen from biomass. J Anal Appl Pyrol 192:107306. https://doi.org/10.1016/j.jaap.2025.107306

36. Zhang Y, Zhang L, Han F et al (2026) Encapsulation of FeCoNiCrMn high-entropy alloy in N-doped carbon fiber as a robust catalyst for boosting sulfur redox kinetics. J Colloid Interface Sci 710:139999. https://doi.org/10.1016/j.jcis.2026.139999
37. Xu J, Liu K, Xue T et al (2025) AlMnCoNiFe high-entropy alloy nanoparticles-embedded carbon cloth: Structure stability and fast charging for lean/anode-free lithium metal batteries. Energy Storage Mater 83:104735. https://doi.org/10.1016/j.ensm.2025.104735
38. Xu X, Guo Y, Bloom BP et al (2020) Elemental core level shift in high entropy alloy nanoparticles *via* X-ray photoelectron spectroscopy analysis and first-principles calculation. ACS Nano 14:17704–17712. https://doi.org/10.1021/acsnano.0c09470
39. Zhang H, Ren T, Bu X et al (2025) Unveiling the heterogeneous structure of FeCoNiPdCu high-entropy alloy: A case study on electrochemical nitrate reduction. Appl Surf Sci 702:163269. https://doi.org/10.1016/j.apsusc.2025.163269
40. Chu J, Bao Y, Li X et al (2021) Characterization of oxidation behavior of Mn fumes generated in the vacuum treatment of melting mn steels. Steel Res Int 92. https://doi.org/10.1002/srin.202000333
41. Das S, Sanjay M, Singh Gautam AR et al (2023) Low bandgap high entropy alloy for visible light-assisted photocatalytic degradation of pharmaceutically active compounds: Performance assessment and mechanistic insights. J Environ Manage 342:118081. https://doi.org/10.1016/j.jenvman.2023.118081
42. Gupta R, Ali H, Verma N (2024) Detection of vanillin in food products over Cu - laser induced graphene nanocomposite using the combined electrochemistry and UV–Vis spectroscopy principles. Microchem J 199:109984. https://doi.org/10.1016/j.microc.2024.109984
43. George JK, Bhagat A, Bhaduri B, Verma N (2023) Carbon nanofiber-bridged carbon nitride-fe2o3 photocatalyst: Hydrogen generation and degradation of aqueous organics. Catal Lett 153:419–431. https://doi.org/10.1007/s10562-022-03985-6
44. Cai J, Han F, Zhang X et al (2026) Hollow carbon sphere-supported high-entropy alloy electrocatalysts enable efficient cascade polysulfide conversion in advanced lithium–sulfur batteries. Electrochim Acta 548:147962. https://doi.org/10.1016/j.electacta.2025.147962
45. Ali H, Gupta R, Verma N (2023) Selective detection of bilirubin in blood serum using UV–Vis spectroelectrochemistry technique with CeO_2-CNF/ITO transparent electrode. Electrochim Acta 468:143159. https://doi.org/10.1016/j.electacta.2023.143159
46. Chen R, Yang H, Jia Y et al (2024) Tuning oxygen vacancies on Bi_2MoO_6 surface for efficient electrocatalytic N_2 reduction reaction. Electrochim Acta 490:144266. https://doi.org/10.1016/j.electacta.2024.144266
47. Tian Y, Liu Y, Wang H et al (2022) Electrocatalytic reduction of nitrogen to ammonia in ionic liquids. ACS Sustain Chem Eng 10:4345–4358. https://doi.org/10.1021/acssuschemeng.2c00018
48. Zhao X, Hu G, Chen G et al (2021) Comprehensive understanding of the thriving ambient electrochemical nitrogen reduction reaction. Adv Mater 33. https://doi.org/10.1002/adma.202007650

49. Wang Z, Li Y, Yu H et al (2018) Ambient electrochemical synthesis of ammonia from nitrogen and water catalyzed by flower-like gold microstructures. Chemsuschem 11:3480–3485. https://doi.org/10.1002/cssc.201801444
50. Chen Z, Wang T (2024) Toward high-performance electrochemical ammonia synthesis by circumventing the surface H-mediated N_2 reduction. JACS Au 4:4023–4031. https://doi.org/10.1021/jacsau.4c00741
51. Yang X, Ling F, Su J et al (2020) Insights into the role of cation vacancy for significantly enhanced electrochemical nitrogen reduction. Appl Catal B 264:118477. https://doi.org/10.1016/j.apcatb.2019.118477
52. Han Z, Wang S, Yang M et al (2026) Electrocatalytic nitrogen fixation and coupling reactions of copper single-atom catalysts. Electrochim Acta 555:148340. https://doi.org/10.1016/j.electacta.2026.148340
53. Tan Y, Wei Y, Liu G et al (2024) Carbon nanotube coated with $FeMoO_4$ composite catalyst for electrochemical nitrogen reduction reaction to ammonia at ambient conditions. Int J Hydrogen Energy 96:723–732. https://doi.org/10.1016/j.ijhydene.2024.11.219
54. Xiong W, Zhou M, Li H et al (2022) Electrocatalytic ammonia synthesis catalyzed by mesoporous nickel oxide nanosheets loaded with Pt nanoparticles. Chin J Catal 43:1371–1378 https://doi.org/10.1016/S1872-2067(21)63877-9

Figures



Figure 1

Schematic representation of the preparation steps for the CFMNC/ACP electrocatalyst. The steps include the incorporation of Cu, Fe, Mn, Ni, and Co metal salts during polymeric bead formation, followed by ball milling and sequential thermal treatments, including carbonization, calcination, activation, and reduction to synthesize CFMNC/ACP.

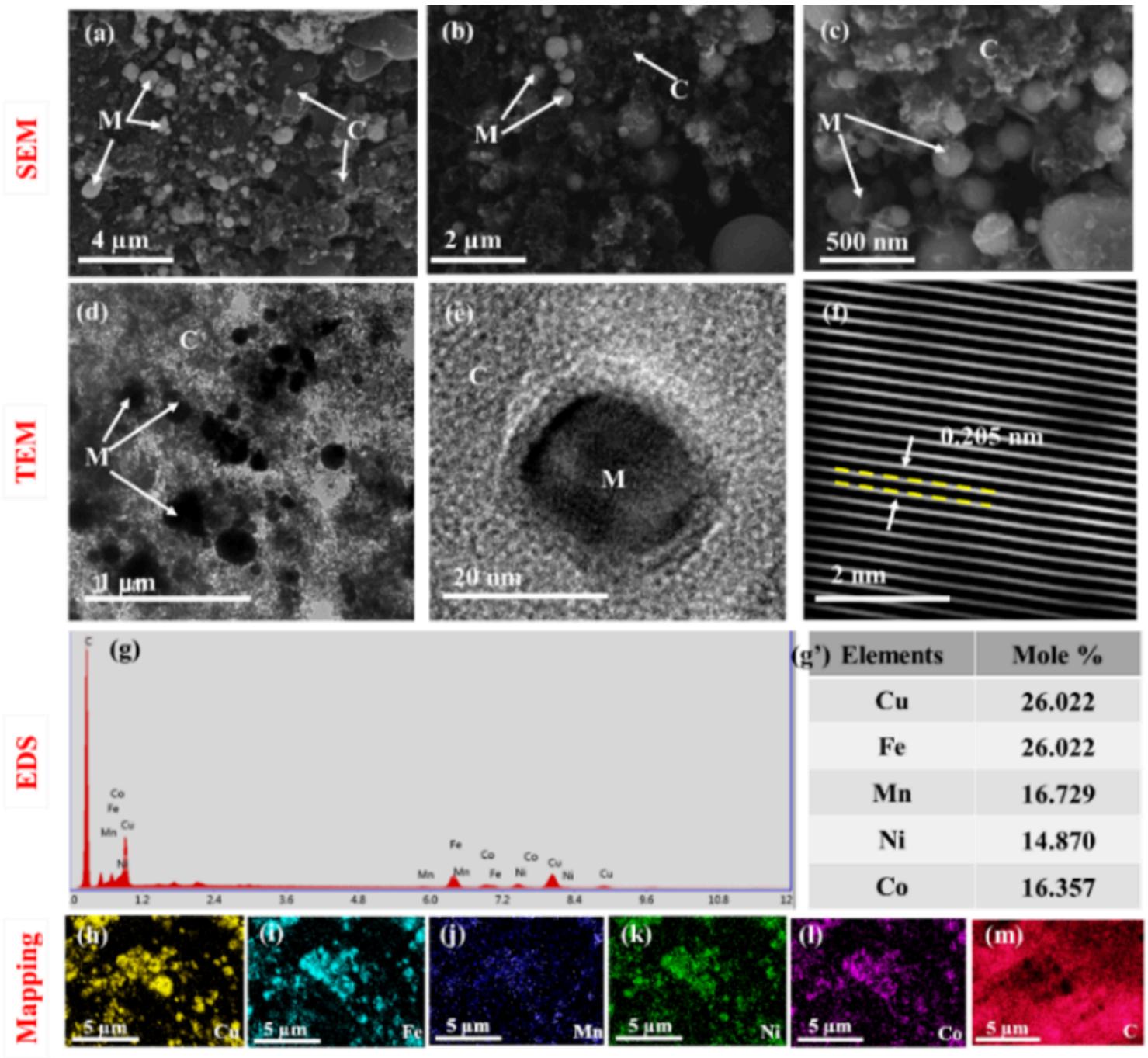

Figure 2

Morphological characterization of CFMNC/ACP; SEM images of CFMNC/ACP with the scale bars of (a) 4 µm, (b) 2 µm, and (c) 500 nm showing spherical CFMNC-HEA NPs anchored on the ACP substrate. (d) TEM image showing the distribution of the relatively darker HEA NPs over ACP. (e) HRTEM image of a HEA NP and (f) the corresponding lattice fringes with the interplanar spacing of ~0.205 nm, assigned to the (1 1 1) crystallographic plane of CFMNC. (g) EDS spectrum and (g') elemental composition in mole percentage. (h-m) Elemental mapping of Cu, Fe, Mn, Ni, Co, and C, respectively. M and C in the micrographs denote metal NPs and ACP, respectively.

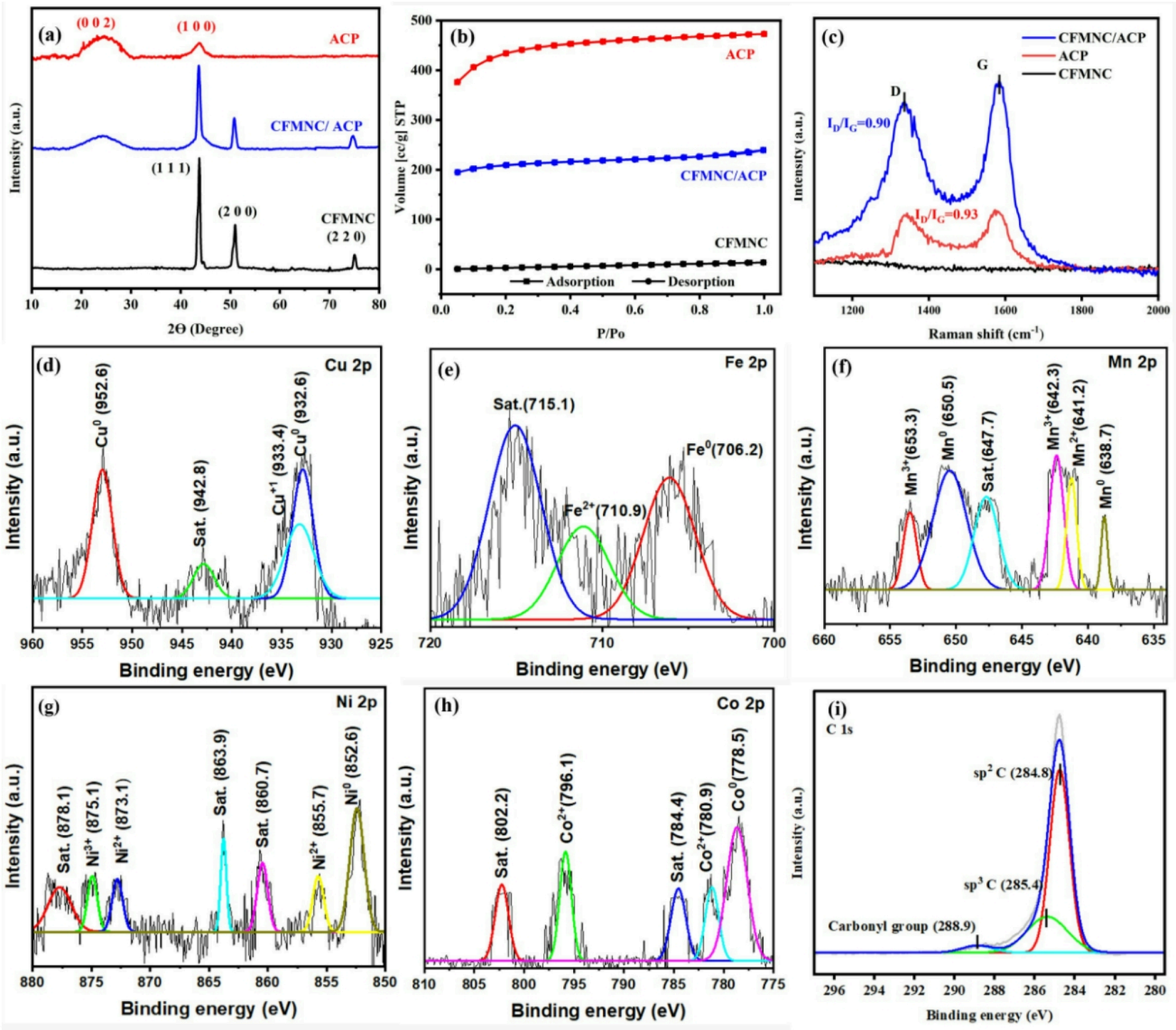

Figure 3

Physicochemical characterization of the materials; (a) XRD patterns of CFMNC, ACP, and CFMNC/ACP, showing the characteristic (1 1 1), (2 0 0), and (2 2 0) diffraction planes of CFMNC and (0 0 2) and (1 0 0) planes of ACP. (b) N_2 adsorption-desorption isotherms of CFMNC, ACP, and CFMNC/ACP, illustrating their textural characteristics and specific surface area. (c) Raman spectra of CFMNC, ACP, and CFMNC/ACP, showing the characteristic disorder-induced D band and graphitic G band of the carbonaceous materials. (d-i) Deconvoluted high-resolution XPS spectra of (d) Cu 2p, (e) Fe 2p, (f) Mn 2p, (g) Ni 2p, (h) Co 2p, and (i) C 1s in CFMNC/ACP, revealing the surface oxidation states and chemical bonding environments of the constituent elements.

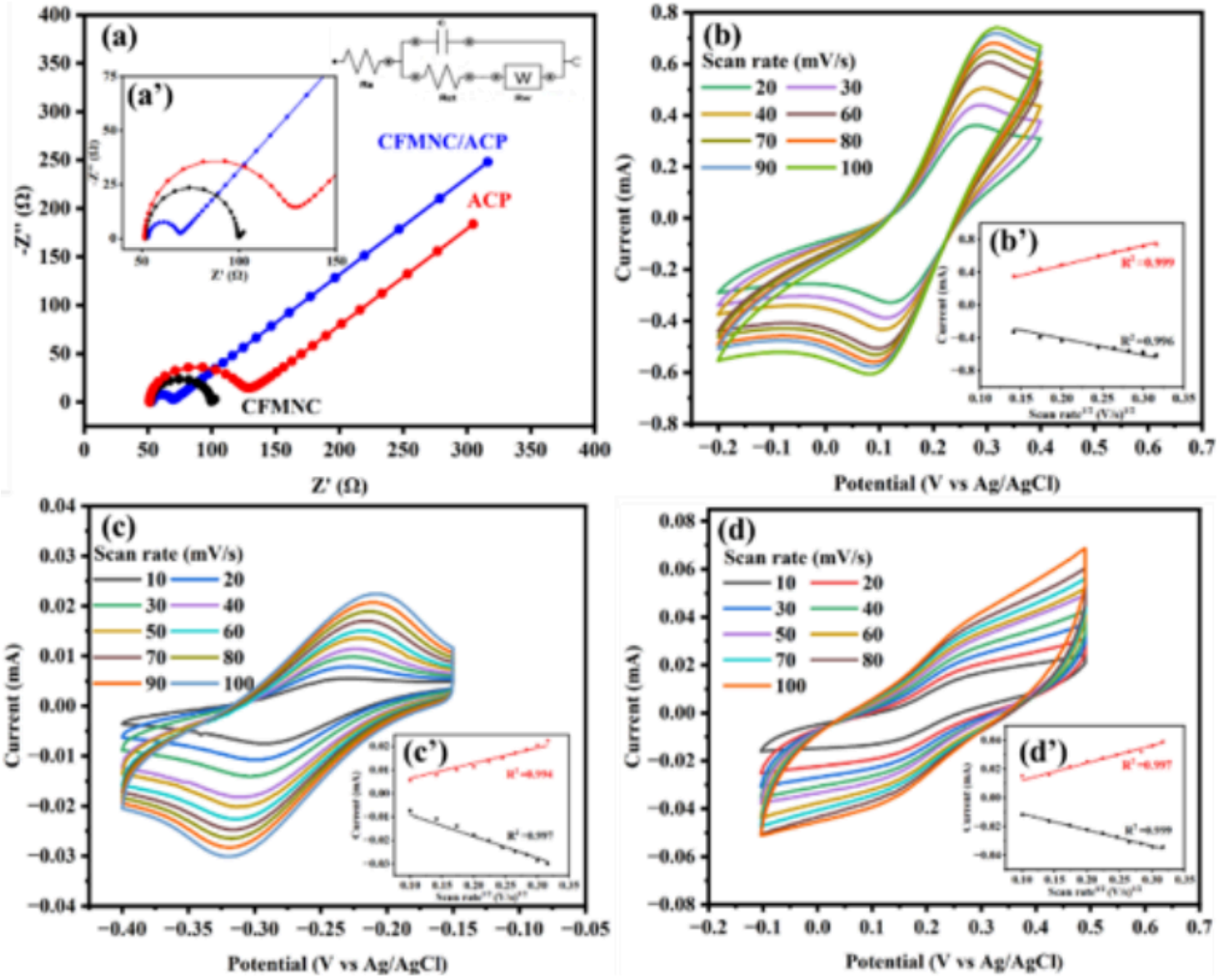

Figure 4

Electrochemical characterization of electrocatalysts: EIS and ECSA analyses; (a) EIS Nyquist plots of the CFMNC, ACP, and CFMNC/ACP electrocatalysts, showing the smallest semicircle for CFMNC/ACP, corresponding to the lowest charge-transfer resistance. (a') Enlarged high-frequency region of the Nyquist plots and the equivalent Randles circuit used for fitting the EIS data. (b-d) CV curves recorded at different scan rates for (b) CFMNC/ACP, (c) ACP, and (d) CFMNC, respectively and (b'-d') Corresponding linear plots of the anodic and cathodic peak currents vs. square root of scan rate, used to determine the ECSA using the Randles-Sevcik equation.

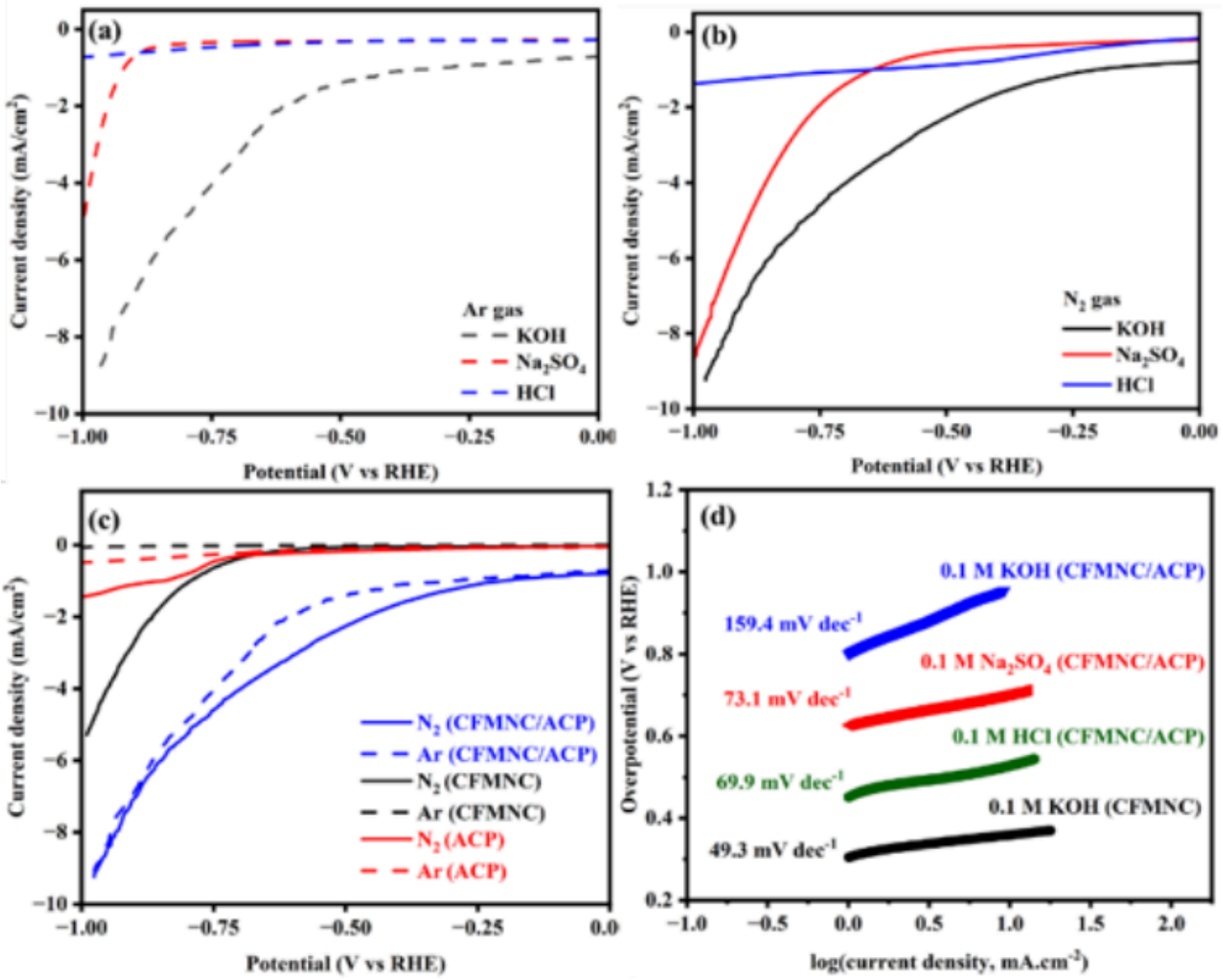

Figure 5

Linear sweep voltammetry and Tafel analysis; LSV curves of CFMNC/ACP in different electrolytes (0.1 M KOH, Na_2SO_4, and HCl) under (a) Ar- and (b) N_2-saturated conditions, illustrating the influence of electrolyte composition and gas atmosphere on the electrocatalytic response. (c) Comparative LSV curves of CFMNC/ACP, CFMNC, and ACP in 0.1 M KOH in Ar- and N_2-saturated conditions, showing the enhanced cathodic current density of CFMNC/ACP in N_2. (d) Tafel plots recorded in Ar-saturated electrolytes, showing the highest Tafel slope for CFMNC/ACP in 0.1 M KOH to indicate the suppressed HER kinetics in the alkaline electrolyte.

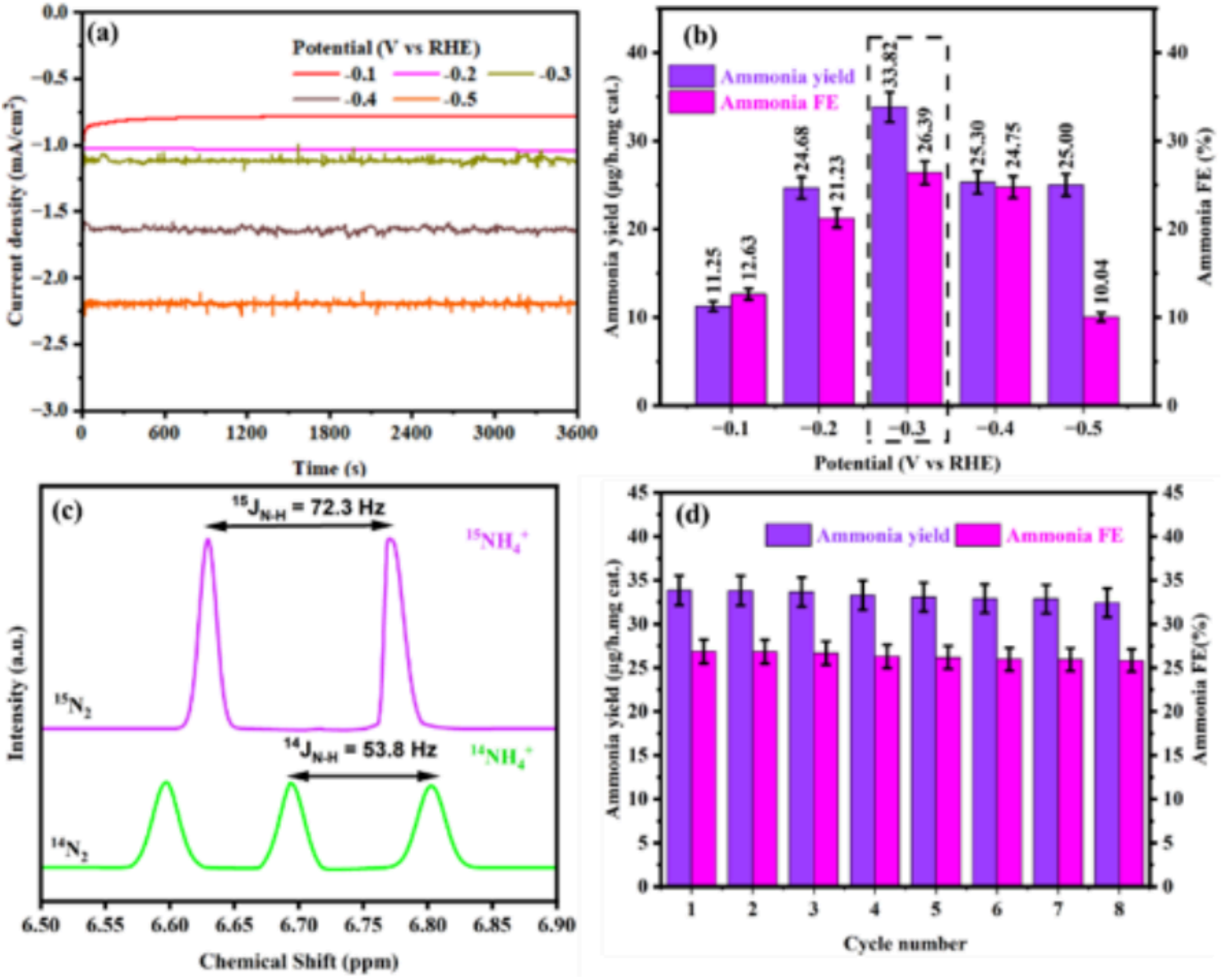

Figure 6

eNRR performance and cyclic stability of the CFMNC/ACP electrocatalyst; (a) Chronoamperometric curves of CFMNC/ACP recorded at different applied potentials (-0.1 to -0.5 V vs. RHE) for 3600 s under N_2-saturated conditions. (b) NH_3 yield and the corresponding FE at different applied potentials, showing the highest NH_3 yield of 33.82 μg h^{-1} mg_{cat}^{-1} and FE of 26.39% at -0.3 V vs. RHE. (c) NMR spectra of the generated ammonium ions using $^{14}N_2$ and $^{15}N_2$ isotopic labeling to confirm the nitrogen source. (d) NH_3 yield and FE over eight consecutive eNRR cycles at -0.3 V vs. RHE, demonstrating a stable electrocatalytic performance throughout the cycles.

Supplementary Files

This is a list of supplementary files associated with this preprint. Click to download.

- floatimage7.png
- SI.docx